

# Family of High-Chern-Number Orbital Magnets in Twisted Rhombohedral Graphene

Xirui Wang<sup>1,\*</sup>, L. Antonio Benítez<sup>1,†</sup>, Võ Tiễn Phong<sup>2,3</sup>, Wai In Chu<sup>1</sup>, Kenji Watanabe<sup>4</sup>, Takashi Taniguchi<sup>5</sup>, Cyprian Lewandowski<sup>2,3</sup>, and Pablo Jarillo-Herrero<sup>1‡</sup>

<sup>1</sup>*Department of Physics, Massachusetts Institute of Technology,  
Cambridge, Massachusetts 02139, USA.*

<sup>2</sup>*Department of Physics, Florida State University, Tallahassee, Florida, 32306, USA.*

<sup>3</sup>*National High Magnetic Field Laboratory, Tallahassee, Florida, 32310, USA.*

<sup>4</sup>*Research Center for Electronic and Optical Materials,  
National Institute for Materials Science,  
1-1 Namiki, Tsukuba 305-0044, Japan. and*

<sup>5</sup>*Research Center for Materials Nanoarchitectonics,  
National Institute for Materials Science,  
1-1 Namiki, Tsukuba 305-0044, Japan.*

## Abstract

Realizing Chern insulators with Chern numbers greater than one remains a major goal in quantum materials research. Such platforms promise multichannel dissipationless chiral transport and access to correlated phases beyond the conventional  $C = 1$  paradigm. Here, we discover a family of high-Chern-number orbital magnets in twisted monolayer–multilayer rhombohedral graphene, denoted  $(1 + n)$  with  $n = 3, 4$ , and  $5$ . Magnetotransport measurements show pronounced anomalous Hall effects at one and three electrons per moiré unit cell when they are polarized away from the moiré interface. Across the  $(1 + n)$  systems, we observe a clear topological hierarchy  $C = n$ , revealed by the Středa trajectories and the quantized Hall resistance. Our experimental observations are supported by self-consistent mean-field calculations. Moreover, we realize both electrical and magnetic switching of the high-Chern-number states by flipping the valley polarization. Together, these results establish a tunable hierarchy of orbital Chern magnets in twisted rhombohedral graphene, offering systematic control of Chern number and topology through layer engineering in pristine graphene moiré systems.

---

<sup>\*</sup> xrwang@mit.edu; These authors contributed equally to this work

<sup>†</sup> lbenitez@mit.edu; These authors contributed equally to this work

<sup>‡</sup> pjarillo@mit.edu

Quantized Hall conductance at zero magnetic field arises when the Berry curvature integrated over the Brillouin zone yields a nonzero, integer-valued Chern number  $C$ . This bulk topological invariant guarantees the existence of chiral edge states, which in turn produce conductance quantized in  $C$  multiples of the conductance quantum. The resulting phase is known as a Chern insulator. Realizing Chern insulators beyond the conventional  $C = 1$  regime opens access to topological phases with multiple co-propagating chiral edge modes, providing a direct route to multi-channel, low-dissipation transport. Moreover, high-Chern-number systems are predicted to host a hierarchy of exotic fractional and non-Abelian excitations [1–8], which emerge from the interplay between strong correlations and topology, and are central to the pursuit to fault-tolerant topological quantum computation [9]. Motivated by this, magnetic topological insulators have shown that  $C$  can be tuned by magnetic doping or layer stacking, thereby establishing a practical design rule for realizing higher-order quantum anomalous Hall states [10].

In parallel, van der Waals heterostructures offer an exciting and versatile platform, with rhombohedral graphene being a particularly promising material candidate, whose valley Chern number increases systematically with the number of layers [11–15]. Moreover, theoretical studies predict that the interlayer hybridization between two twisted rhombohedral multilayers enables the design of Chern bands with tunable topology via displacement field and twist angle, as well as allowing the Chern number to be selected by appropriate layer combinations [16–18]. This approach provides a powerful route to design and control topological band structures, yet experimental realizations of such high-Chern-number moiré systems have only recently begun to emerge [19–21]. Importantly, these systems can go beyond the graphene–hBN moiré paradigm, where the broken inversion symmetry in hBN has a strong influence on the electronic properties of rhombohedral graphene but the exact mechanism remains incompletely understood [22].

In this work, we engineer a family of twisted monolayer–multilayer rhombohedral graphene (multi-RhG) structures, denoted  $(1 + n)$ , to systematically study how the Chern number evolves as we increase the number of layers. By applying a small twist angle between monolayer and multi-RhG flakes from the same parent crystal, we create a well-defined moiré potential at the interface, enabling controlled exploration and engineering of topological band structures.

## I. BAND STRUCTURE EVOLUTION WITH DISPLACEMENT FIELD

The device schematic and an optical image of a representative device are shown in Fig. 1a,b. The device consists of a multi-RhG with a monolayer graphene (Gr) placed on top, forming a twist angle  $\theta$  and thereby generating a moiré pattern characterized by moiré wavelength  $\lambda$ . We encapsulate the  $(1+n)$  stack with hBN dielectrics, and intentionally misalign them with the graphene lattice to prevent the formation of secondary moiré structures. To this end, we perform lateral force microscopy (LFM) with atomic resolution on both the graphene and hBN flakes. For example, the graphene is misaligned by approximately  $30^\circ$  and  $20^\circ$  from top and bottom hBN, respectively, as shown in Fig. 1b for a twisted  $(1+3)$  device. Outside the hBN layers, we use top and bottom graphite gates to independently control the displacement field  $D$  and carrier density  $n$ . We confirm the rhombohedral stacking order of the multilayer graphene by Raman mapping (see Methods and Extended Data Fig. 2 and Fig. 3), before patterning the stack into a Hall-bar geometry for measuring the longitudinal ( $R_{xx}$ ) and transverse ( $R_{yx}$ ) resistances.

According to the single-particle band structure calculations in Fig. 1c, in the absence of a perpendicular displacement field  $D$ , the low-energy states of the  $(1+n)$  system are intrinsically layer-unpolarized. The monolayer graphene is labeled as layer  $n+1$ , and the layer index of multi-RhG stack is denoted by  $1, 2, \dots, n$  ( $n = 3, 4$ , or  $5$ ). For  $\Delta = -20$  meV ( $D < 0$ , relation between  $\Delta$  and  $D$  is explained in Supplementary Information), the first conduction band flattens and becomes nearly fully polarized toward the bottom layer of the multi-RhG, while carrying a nontrivial Chern number ( $C \neq 0$ ). The calculation in Fig. 1c corresponds to a  $(1+3)$  system with a twist angle of  $1.3^\circ$ , though a similar behavior occurs for  $(1+3)$ ,  $(1+4)$  and  $(1+5)$  structures, predicting a Chern number of  $3, 4$  and  $5$  at moderate negative displacement fields, respectively (see Extended Data Fig. 9 and Supplementary Figs. S1-S3). The strong electronic interactions due to the flatness of the conduction band are expected to split the band and generate a cascade of correlated phases (see Supplementary Information). At  $\Delta = 20$  meV ( $D > 0$ ), the first conduction band wave function becomes polarized toward the moiré interface. The pronounced band dispersion around the  $\bar{\Gamma}$  point indicates that the kinetic energy dominates, thereby suppressing electron-electron correlation effects. By varying  $D$ , one can thus continuously drive the system between distinct electronic configurations, ranging from flat, layer-polarized bands with non-trivial topology and strong

interaction effects, to more dispersive, weakly correlated regimes. Figure 1d schematically illustrates this evolution, highlighting the position of the wave functions either close to the moiré interface for  $D > 0$  or farther from it for  $D < 0$ .

## II. HIGH-CHERN-NUMBER QUANTUM ANOMALOUS HALL EFFECT IN TWISTED $(1 + n)$ GRAPHENE

To reveal the electronic behavior of the  $(1 + n)$  systems, Fig. 2 presents  $R_{xx}$  and  $R_{yx}$  maps as functions of the filling factor  $\nu$  and the displacement field  $D$ , for  $n = 3, 4$ , and  $5$  (information and images of all the devices in this study are shown in Extended Data Table 1 and Extended Data Fig. 1). Throughout this work,  $R_{xx}$  and  $R_{yx}$  denote the symmetrized and antisymmetrized components of the raw resistance data with respect to magnetic field, unless otherwise specified.  $R_{xx}$  exhibits insulating behavior at full fillings of conduction and valence bands, reflecting the band insulator formed from the moiré band folding. Near charge neutrality, the system develops a gap as  $D$  increases, while on the hole side,  $R_{xx}$  remains metallic for all  $D$ , consistent with our band structure calculations (Fig. 1c). On the electron side, and particularly for negative  $D$  which corresponds to states away from the moiré interface, the  $R_{xx}$  maps display pronounced resistive peaks close to integer fillings  $\nu = 1, 2$ , and  $3$ , indicating tunable symmetry breaking and strong correlation effects. The corresponding  $R_{yx}$  maps (Fig. 2d-f) show clear  $R_{yx}$  hot spots near  $\nu = 1$  and  $\nu = 3$  for  $D < 0$ . Notably, the hot spot near  $\nu = 1$  is highly reproducible across the different  $(1 + n)$  systems. Around  $\nu = 3$  for the  $(1 + 3)$  and  $(1 + 4)$  devices,  $R_{yx}$  exhibits sign reversals as either  $D$  or  $\nu$  is tuned, indicating a doping- and displacement-field-controlled reversal of the sign of the Berry curvature, which will be discussed later on in detail.

To gain further insight into the  $R_{yx}$  hot spots, Fig. 3a-c present detailed maps of  $R_{yx}$  for electron doping and  $D < 0$ . To verify their magnetic character, Fig. 3d-f show  $R_{xx}$  (blue) and  $R_{yx}$  (black) as functions of the out-of-plane magnetic field  $B$  at selected values of  $\nu$  and  $D$ . At  $\nu \approx 1$ , the  $(1 + 3)$ ,  $(1 + 4)$ , and  $(1 + 5)$  devices exhibit similar responses with prominent anomalous Hall signals as well as hysteresis as  $B$  is scanned forward and backward. In the  $(1 + 5)$  device,  $R_{yx}$  develops a quantized plateau corresponding to  $C = 5$ , indicative of a high-Chern-number quantum anomalous Hall state. We also observe a region of  $R_{yx}$  hot spots between  $\nu = 1$  and  $\nu = 2$  that disperse with both  $\nu$  and  $D$  in the  $(1 + 5)$  device,

resembling features previously reported in rhombohedral graphene aligned with hBN [23]. Furthermore, the requirement of a higher displacement field to observe the anomalous Hall effect in the (1 + 5) device compared to (1 + 3) and (1 + 4) suggests enhanced electrostatic screening with increasing layer number [24].

### III. ELECTRICAL AND MAGNETIC SWITCHING OF HIGH-CHERN-NUMBER ORBITAL MAGNETS

To reveal the underlying band topology, we performed measurements at higher magnetic fields. In general, the Hall resistance plateau of an incompressible Chern insulator follows the dispersion  $C = \frac{h}{e} \frac{\partial n}{\partial B}$  according to the Středa relation [25], which links the change in carrier density with magnetic field to the Chern number  $C$ . In the twisted (1 + 3) device, the Hall plateau at  $\nu = 1$  shifts with magnetic field with a slope corresponding to  $C = 3$  as shown in Fig. 4a (dotted line as a guide to the eye). A line cut along this  $C = 3$  trajectory is presented in Fig. 4c, showing that  $R_{yx}$  begins to saturate near 4 T at a value close to  $|R_{yx}| = h/3e^2$  (slightly higher), consistent with a Chern number of 3 predicted by our calculations (Fig. 1c). This observation indicates that electrons are polarized into a single valley as a result of strong electron-electron interactions. In addition to the  $\nu = 1$  dispersion, we observe an  $R_{yx}$  hot spot emerging near  $\nu = 1.5$ , following a dispersion consistent with a Chern number  $C = 2$  (Fig. 4a). Similar integer anomalous Hall features at fractional fillings have been reported in moiré graphene systems, arising from the doubling of the moiré unit cell driven by electron correlations (*e.g.* charge density wave) [26, 27]. The measured Chern number depends on the Berry curvature distribution across the reconstructed band and can yield folded subbands carrying a Chern number smaller than or equal to that of the parent band [26, 27]. There is also the possibility that this state is more exotic, *i.e.* cannot be described by a mean-field framework, given that it occurs at partial fillings of a band [28]. At  $\nu = 3$ , shown in Fig. 4e, the  $R_{yx}$  hot spot disperses along approximately  $C = -3$ , indicating that the electrons now occupy the opposite valley compared to  $\nu = 1$ . Another (1 + 3) device exhibiting quantized  $R_{yx}$  around  $\nu = 3$  near zero  $B$  is shown in Extended Data Fig. 5.

In the (1 + 4) device, we observe a Středa slope of  $C = 4$  from  $\nu = 1$ , and  $C = -4$  from  $\nu = 3$ , anticipated by band structure calculations (Extended Data Fig. 6 and Fig. 9). The  $R_{yx}$  is not quantized probably due to the moiré disorder in the sample [29]. In a (1 + 5)

device, we observe the  $R_{yx}$  dispersion emanating from  $\nu = 1$  with a slope corresponding to  $C = 5$ , as shown in Fig. 4b, aligning with the measured quantized  $|R_{yx}| = h/5e^2$  (Fig. 4c). Single-particle band calculations predict a flat conduction band with  $C = 5$ . Incorporating electron–electron interactions within a self-consistent Hartree–Fock framework yields a spin–valley–polarized state preserving the same topological character, indicating that the essential physics is already encoded in the single-particle description (Fig. 4d and Extended Data Fig. 9). The calculated band structure further reveals that the electronic states are localized in layers distant from the moiré interface (Extended Data Fig. 9), similar to the behavior predicted in the twisted  $(1 + 3)$  device. At magnetic fields above 0.5 T, an additional dispersing feature appears, which likely originates from conventional Landau-level formation. Another  $R_{yx}$  hot spot dispersing from  $\nu \approx 1.5$  corresponds to the hot-spot region between  $\nu = 1$  and  $\nu = 2$  observed in Fig. 2f and Fig. 3c.

We also note that, as the magnetic field increases above 0.5 T,  $R_{yx}$  becomes negative at  $\nu = 3 + \delta$  while remaining positive at  $\nu = 3 - \delta$  in the  $(1 + 3)$  device, and a similar behavior is seen at  $\nu = 1$  as well as in twisted  $(1 + 4)$  and  $(1 + 5)$  samples (Fig. 4a,b and Extended Data Fig. 6). Given the small spin magnetization in the moiré system, we can understand the doping-induced  $R_{yx}$  sign switching behavior from the competition between bulk and edge orbital currents. The former comes from self-rotation of the wave packet which evolves within the band, and the latter is from chiral edge currents when the Fermi level lies within a Chern gap [29–32]. Since  $K$  and  $K'$  valleys have opposite Berry curvature, a flip of the  $R_{yx}$  sign corresponds to the change of polarization between the two valleys. We examine three representative linecuts with different sequences of  $R_{yx}$  sign reversals using the schematic in Fig. 4g. The corresponding examples are denoted as linecuts in the dual-gate map of the  $(1 + 3)$  device (Fig. 3a). As the doping evolves from  $\nu = 0$  or 2 towards  $\nu = 1$  or 3,  $R_{yx}$  either stays negative (black line), positive (green line), or change from positive to negative (yellow line). The total magnetization  $m_{\text{total}}$  from either  $K$  (red) or  $K'$  (purple) valleys are plotted as a function of doping.

The system tends to minimize the Zeeman energy by aligning the total magnetization with the external magnetic field. In a single valley, bulk and edge contributions are opposite in sign, with the values depending on the details of the Berry curvature distribution or the Chern gap size. As a result, their total contribution in magnetization may or may not change sign as Fermi level goes across the Chern gap. When the total magnetization of

a single valley changes sign, the system tends to switch valleys to maintain low Zeeman energy, leading to a reversal of  $R_{yx}$  (yellow line). In the well-quantized (1 + 5) device, this enables electrical switching of the high Chern number, as shown in Extended Data Fig. 7. On the other hand, if the sign of the total magnetization of a single valley remains the same (green line), or if the gain in Zeeman energy does not overcome the energy barrier to flip the valley (black line), the system remains polarized to the same valley. This framework also explains the field-dependent sign reversal, where a high magnetic field tilts the energy landscape between  $K$  and  $K'$  valleys, so that a sign reversal is observed which otherwise does not occur at small  $B$ . Doping-induced valley switching is accompanied by pronounced hysteresis as carrier density is swept forward and backward (Fig. 4f, Extended Data Fig. 4 and Fig. 7). This indicates that the valley switching occurs via a first-order phase transition probably due to domain-wall pinning between regions harboring opposite valley polarization. The divergence of the coercive magnetic field around  $\nu = 1$  or 3 further suggests a minimal energy splitting between the  $K$  and  $K'$  valleys [32].

#### IV. CONCLUSION

Our experiments establish the twisted (1 +  $n$ ) family of graphene moiré systems as a promising platform for engineering high-Chern-number bands via controlled combinations of rhombohedral layer number, in a range of twist angles with high reproducibility (Extended Data Fig. 4, Fig. 5, and Fig. 7). Despite the substantial differences among tri-, tetra-, and penta-layer rhombohedral graphene, their behavior when interfaced with monolayer graphene is remarkably similar. All exhibit robust, and in some cases quantized, anomalous Hall effects at filling factors of one and three electrons per moiré unit cell, occurring when electrons localize in the layer farthest from the moiré interface—analogous to the behavior observed in rhombohedral graphene aligned with hBN [33–41].

It is instructive to compare our results with multi-RhG aligned to hBN. In that case, alignment produces an isolated flat Chern band with  $C = 1$ , independent of layer number, in contrast to our twisted 1+ $n$  systems where the Chern number scales with the rhombohedral block thickness. We note that in our case, the mono/multi-RhG twist interface provides a well-defined moiré potential free from the sublattice ambiguity of hBN, allowing a straightforward comparison with theoretical calculations. In fact, the observed layer-

dependent Chern hierarchy is in agreement with predictions of single-particle band model calculations, which remain qualitatively unchanged after introduction of Coulomb interactions at a mean-field level. These findings highlight the distinct roles of moiré potential and interlayer hybridization in determining topological band structures in graphene-based systems.

Moving forward, it is interesting to explore smaller twist angles especially in (1 + 4) and (1 + 5) systems, where it has been shown that fractional states more likely emerge at a large moiré wavelength in RhG/hBN systems [42]. Future extensions to multilayer configurations such as 2+3, 2+4, or 2+5 rhombohedral graphene will be particularly intriguing, as bilayer or thicker rhombohedral graphene can host isolated flat bands tunable by displacement field, providing a promising route to further enhance correlations in the topological bands [18]. These systems could offer an ideal setting for realizing fractional states in high-Chern-number bands. Furthermore, given the plethora of unconventional superconductivity observed in rhombohedral graphene [24, 43–48], creating lateral junctions to couple high-Chern-number insulators with superconductivity could open new opportunities for non-Abelian statistics and topological superconductivity [38, 49].

*Note: During the preparation of this manuscript, we became aware of a related study on twisted 1+5 rhombohedral graphene [21].*

---

- [1] Y.-F. Wang, H. Yao, C.-D. Gong, and D. N. Sheng, Phys. Rev. B **86**, 201101 (2012).
- [2] M. Barkeshli and X.-L. Qi, Phys. Rev. X **2**, 031013 (2012).
- [3] Z. Liu, E. J. Bergholtz, H. Fan, and A. M. Läuchli, Phys. Rev. Lett. **109**, 186805 (2012).
- [4] A. Sterdyniak, C. Repellin, B. A. Bernevig, and N. Regnault, Phys. Rev. B **87**, 205137 (2013).
- [5] T. Liu, C. Repellin, B. A. Bernevig, and N. Regnault, Phys. Rev. B **87**, 205136 (2013).
- [6] G. Möller and N. R. Cooper, Phys. Rev. Lett. **115**, 126401 (2015).
- [7] B. Andrews and G. Möller, Phys. Rev. B **97**, 035159 (2018).
- [8] B. Andrews, T. Neupert, and G. Möller, Phys. Rev. B **104**, 125107 (2021).
- [9] C. Nayak, S. H. Simon, A. Stern, M. Freedman, and S. Das Sarma, Rev. Mod. Phys. **80**, 1083 (2008).
- [10] Y.-F. Zhao, R. Zhang, R. Mei, L.-J. Zhou, H. Yi, Y.-Q. Zhang, J. Yu, R. Xiao, K. Wang,

N. Samarth, *et al.*, *Nature* **588**, 419 (2020).

[11] H. Zhou, T. Xie, A. Ghazaryan, T. Holder, J. R. Ehrets, E. M. Spanton, T. Taniguchi, K. Watanabe, E. Berg, M. Serbyn, *et al.*, *Nature* **598**, 429 (2021).

[12] T. Han, Z. Lu, G. Scuri, J. Sung, J. Wang, T. Han, K. Watanabe, T. Taniguchi, H. Park, and L. Ju, *Nat. Nanotechnol.* **19**, 181 (2024).

[13] K. Liu, J. Zheng, Y. Sha, B. Lyu, F. Li, Y. Park, Y. Ren, K. Watanabe, T. Taniguchi, J. Jia, *et al.*, *Nat. Nanotechnol.* **19**, 188 (2024).

[14] T. Han, Z. Lu, Y. Yao, J. Yang, J. Seo, C. Yoon, K. Watanabe, T. Taniguchi, L. Fu, F. Zhang, *et al.*, *Science* **384**, 647 (2024).

[15] Y. Sha, J. Zheng, K. Liu, H. Du, K. Watanabe, T. Taniguchi, J. Jia, Z. Shi, R. Zhong, and G. Chen, *Science* **384**, 414 (2024).

[16] P. J. Ledwith, A. Vishwanath, and E. Khalaf, *Phys. Rev. Lett.* **128**, 176404 (2022).

[17] J. Wang and Z. Liu, *Phys. Rev. Lett.* **128**, 176403 (2022).

[18] V. T. Phong and C. Lewandowski, Preprint at <https://arxiv.org/abs/2505.07981> (2025).

[19] J. Dong, L. Liu, J. Zhu, Z. Pan, Y. Hong, Z. Jia, K. Watanabe, T. Taniguchi, L. Du, D. Shi, *et al.*, Preprint at <https://arxiv.org/abs/2507.09908> (2025).

[20] W. Wang, Y. Wang, Z. Zhang, Z. Huo, G. Zhou, K. Watanabe, T. Taniguchi, X. Xie, K. Liu, Z. Song, *et al.*, Preprint at <https://arxiv.org/abs/2507.10875> (2025).

[21] N. Liu, Z. Chen, J. Ding, W. Zhou, H. Xiang, X. Fang, L. Wu, X. Zhan, L. Zhang, Q. Chen, *et al.*, Preprint at <https://arxiv.org/abs/2507.11347> (2025).

[22] M. Uzan, W. Zhi, M. Bocarsly, J. Dong, S. Dutta, N. Auerbach, N. S. Kander, M. Labendik, Y. Myasoedov, M. E. Huber, *et al.*, Preprint at <https://arxiv.org/abs/2507.20647> (2025).

[23] J. Zheng, S. Wu, K. Liu, B. Lyu, S. Liu, Y. Sha, Z. Li, K. Watanabe, T. Taniguchi, J. Jia, *et al.*, Preprint at <https://arxiv.org/abs/2412.09985> (2024).

[24] M. Kumar, D. Waleffe, A. Okounkova, R. Tejani, V. T. Phong, K. Watanabe, T. Taniguchi, C. Lewandowski, J. Folk, and M. Yankowitz, Preprint at <https://arxiv.org/abs/2507.18598> (2025).

[25] P. Streda, *J. Phys. C: Solid State Phys.* **15**, L1299 (1982).

[26] H. Polshyn, Y. Zhang, M. A. Kumar, T. Soejima, P. Ledwith, K. Watanabe, T. Taniguchi, A. Vishwanath, M. P. Zaletel, and A. F. Young, *Nat. Phys.* **18**, 42 (2022).

[27] Y. Xie, A. T. Pierce, J. M. Park, D. E. Parker, E. Khalaf, P. Ledwith, Y. Cao, S. H. Lee,

S. Chen, P. R. Forrester, *et al.*, *Nature* **600**, 439 (2021).

[28] T. Tan, J. May-Mann, and T. Devakul, Preprint at <https://arxiv.org/abs/2409.06775> (2024).

[29] S. Grover, M. Bocarsly, A. Uri, P. Stepanov, G. Di Battista, I. Roy, J. Xiao, A. Y. Meltzer, Y. Myasoedov, K. Pareek, *et al.*, *Nat. Phys.* **18**, 885 (2022).

[30] H. Polshyn, J. Zhu, M. A. Kumar, Y. Zhang, F. Yang, C. L. Tschirhart, M. Serlin, K. Watanabe, T. Taniguchi, A. H. MacDonald, *et al.*, *Nature* **588**, 66 (2020).

[31] J. Zhu, J.-J. Su, and A. H. MacDonald, *Phys. Rev. Lett.* **125**, 227702 (2020).

[32] C. Tschirhart, M. Serlin, H. Polshyn, A. Shragai, Z. Xia, J. Zhu, Y. Zhang, K. Watanabe, T. Taniguchi, M. Huber, *et al.*, *Science* **372**, 1323 (2021).

[33] Z. Lu, T. Han, Y. Yao, A. P. Reddy, J. Yang, J. Seo, K. Watanabe, T. Taniguchi, L. Fu, and L. Ju, *Nature* **626**, 759 (2024).

[34] J. Xie, Z. Huo, X. Lu, Z. Feng, Z. Zhang, W. Wang, Q. Yang, K. Watanabe, T. Taniguchi, K. Liu, *et al.*, *Nat. Mater.* **24**, 1042 (2025).

[35] D. Waters, A. Okounkova, R. Su, B. Zhou, J. Yao, K. Watanabe, T. Taniguchi, X. Xu, Y.-H. Zhang, J. Folk, *et al.*, *Phys. Rev. X* **15**, 011045 (2025).

[36] S. H. Aronson, T. Han, Z. Lu, Y. Yao, J. P. Butler, K. Watanabe, T. Taniguchi, L. Ju, and R. C. Ashoori, *Phys. Rev. X* **15**, 031026 (2025).

[37] Z. Wang, Q. Liu, X. Han, Z. Li, W. Zhao, Z. Qu, C. Han, K. Watanabe, T. Taniguchi, Z. V. Han, *et al.*, Preprint at <https://arxiv.org/abs/2503.00837> (2025).

[38] Y. Choi, Y. Choi, M. Valentini, C. L. Patterson, L. F. Holleis, O. I. Sheekey, H. Stoyanov, X. Cheng, T. Taniguchi, K. Watanabe, *et al.*, *Nature* **639**, 342 (2025).

[39] C. Li, Z. Sun, K. Liu, L. Qiao, Y. Wei, C. Zheng, C. Zhang, K. Watanabe, T. Taniguchi, H. Yang, *et al.*, Preprint at <https://arxiv.org/abs/2505.01767> (2025).

[40] W. Zhou, J. Ding, J. Hua, L. Zhang, K. Watanabe, T. Taniguchi, W. Zhu, and S. Xu, *Nat. Commun.* **15**, 2597 (2024).

[41] J. Ding, H. Xiang, J. Hua, W. Zhou, N. Liu, L. Zhang, N. Xin, B. Wu, K. Watanabe, T. Taniguchi, *et al.*, *Phys. Rev. X* **15**, 011052 (2025).

[42] Z. Huo, W. Wang, J. Xie, Y. H. Kwan, J. Herzog-Arbeitman, Z. Zhang, Q. Yang, M. Wu, K. Watanabe, T. Taniguchi, *et al.*, Preprint at <https://arxiv.org/abs/2510.15309> (2025).

[43] J. Seo, A. A. Cotten, M. Xu, O. S. Sedeh, H. Weldeyesus, T. Han, Z. Lu, Z. Wu, S. Ye, W. Xu, *et al.*, Preprint at <https://arxiv.org/abs/2509.03295> (2025).

- [44] E. Morissette, P. Qin, H.-T. Wu, N. J. Zhang, K. Watanabe, T. Taniguchi, and J. Li, Preprint at <https://arxiv.org/abs/2504.05129> (2025).
- [45] R. Q. Nguyen, H.-T. Wu, E. Morissette, N. J. Zhang, P. Qin, K. Watanabe, T. Taniguchi, A. W. Hui, D. E. Feldman, and J. Li, Preprint at <https://arxiv.org/abs/2507.22026> (2025).
- [46] J. Deng, J. Xie, H. Li, T. Taniguchi, K. Watanabe, J. Shan, K. F. Mak, and X. Liu, Preprint at <https://arxiv.org/abs/2508.15909> (2025).
- [47] M. Kumar, D. Waleffe, A. Okounkova, R. Tejani, K. Watanabe, T. Taniguchi, É. Lantagne-Hurtubise, J. Folk, and M. Yankowitz, Preprint at <https://arxiv.org/abs/2511.16578> (2025).
- [48] Y. Guo, O. I. Sheekey, T. Arp, K. Kolář, T. Charpentier, L. Holleis, B. Foutty, A. Keough, M. Kang-Chou, M. E. Huber, *et al.*, Preprint at <https://arxiv.org/abs/2511.17423> (2025).
- [49] J. Röntynen and T. Ojanen, Phys. Rev. Lett. **114**, 236803 (2015).

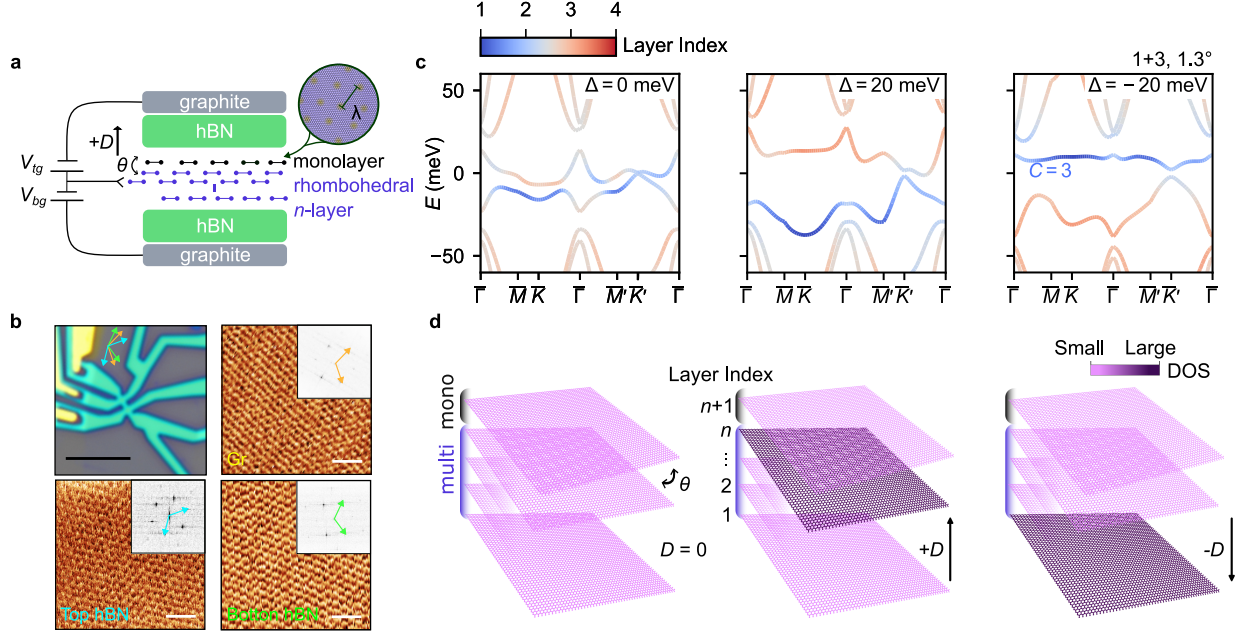


**Figure 1. Device structure, moiré characterization, and band structure calculations in twisted  $(1+n)$  systems.** **a**, Schematic of a twisted  $(1+n)$  heterostructure, consisting of a monolayer graphene placed on an  $n$ -layer rhombohedral graphene with a twist angle  $\theta$ , forming a moiré superlattice of wavelength  $\lambda$ . Top and bottom graphite gates enable independent control of carrier density  $n$  and displacement field  $D$ . **b**, Optical micrograph (top left) of a typical device used in this study, and lateral force microscopy (LFM) images of graphene (Gr) and top and bottom hexagonal boron nitride (hBN) lattices. The Fourier transform insets reveal the threefold or sixfold symmetry of the atomic lattices, with armchair directions indicated. The scale bars correspond to 5  $\mu\text{m}$  in the optical image and 1 nm in the LFM images. **c**, Single-particle band structures of twisted  $(1+3)$  graphene at  $\theta = 1.3^\circ$  at interlayer potential differences  $\Delta$  of 0, 20, and  $-20$  meV. At  $\Delta = -20$  meV, the first conduction band has  $C = 3$ . The color represents layer polarization, with 4-red (1-blue) indicating charge localization on the monolayer (multilayer away from moiré interface) side. **d**, Schematic illustration of the evolution of layer polarization with  $D$ , showing electronic states localized near the moiré interface for  $D > 0$  and shifted toward the bottom multilayer surface for  $D < 0$ . DOS: Density of states.

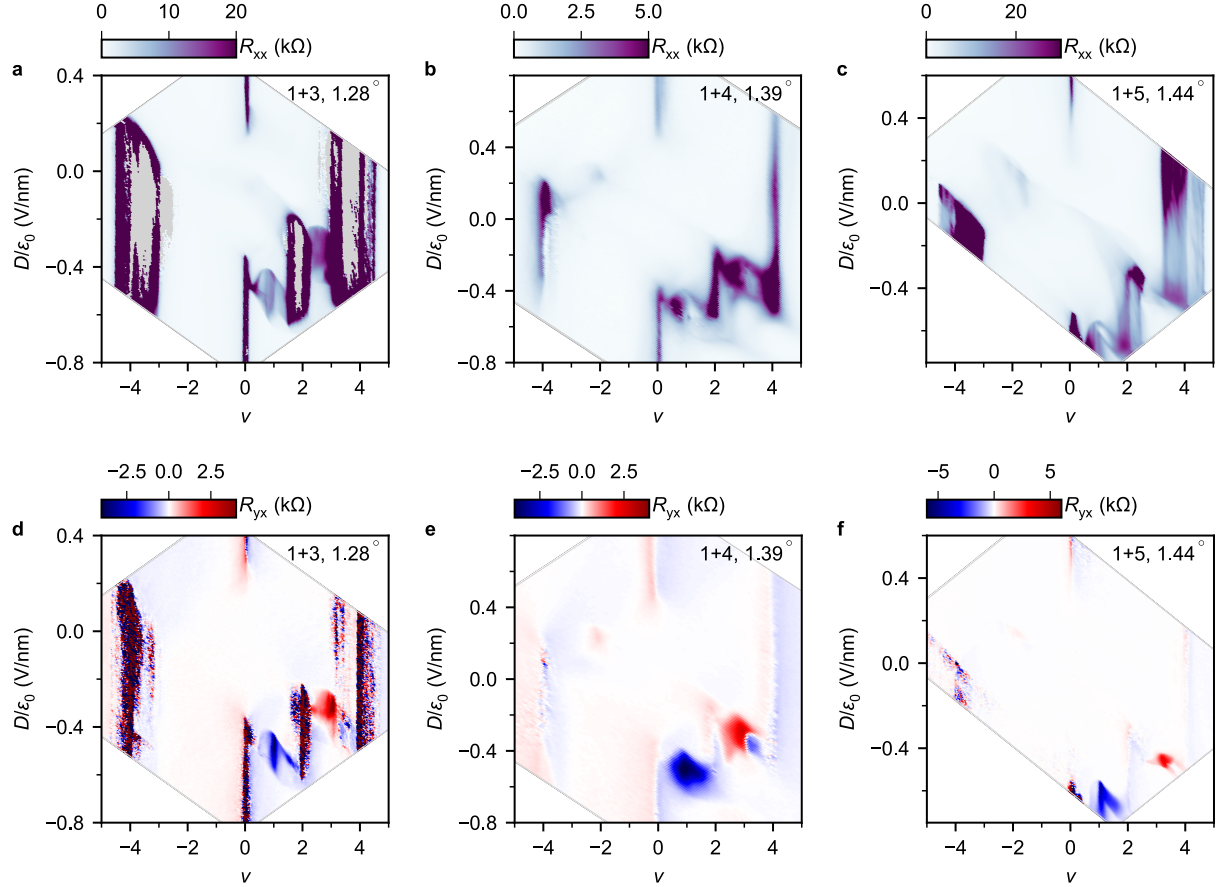


**Figure 2. Longitudinal and transverse resistance maps of  $(1+n)$  systems.** **a-c**, Longitudinal resistance  $R_{xx}$  as a function of filling factor  $\nu$  and displacement field  $D/\varepsilon_0$  for  $(1+3)$ ,  $(1+4)$ , and  $(1+5)$  devices with twist angles of  $1.28^\circ$ ,  $1.39^\circ$ , and  $1.44^\circ$ , respectively. All the data of  $(1+3)$  and  $(1+4)$  devices in the main figures are from the same devices as in **a,b**. **d-f**, Corresponding dual-gate maps of transverse resistance  $R_{yx}$  for the same devices. Data were taken at out-of-plane magnetic field  $B = 0.1$  T,  $0.2$  T, and  $0.06$  T for  $(1+3)$ ,  $(1+4)$ , and  $(1+5)$  devices, respectively, with  $R_{xx}$  data symmetrized and  $R_{yx}$  antisymmetrized with respect to  $B$ . All data were taken at  $T = 0.3$  K.

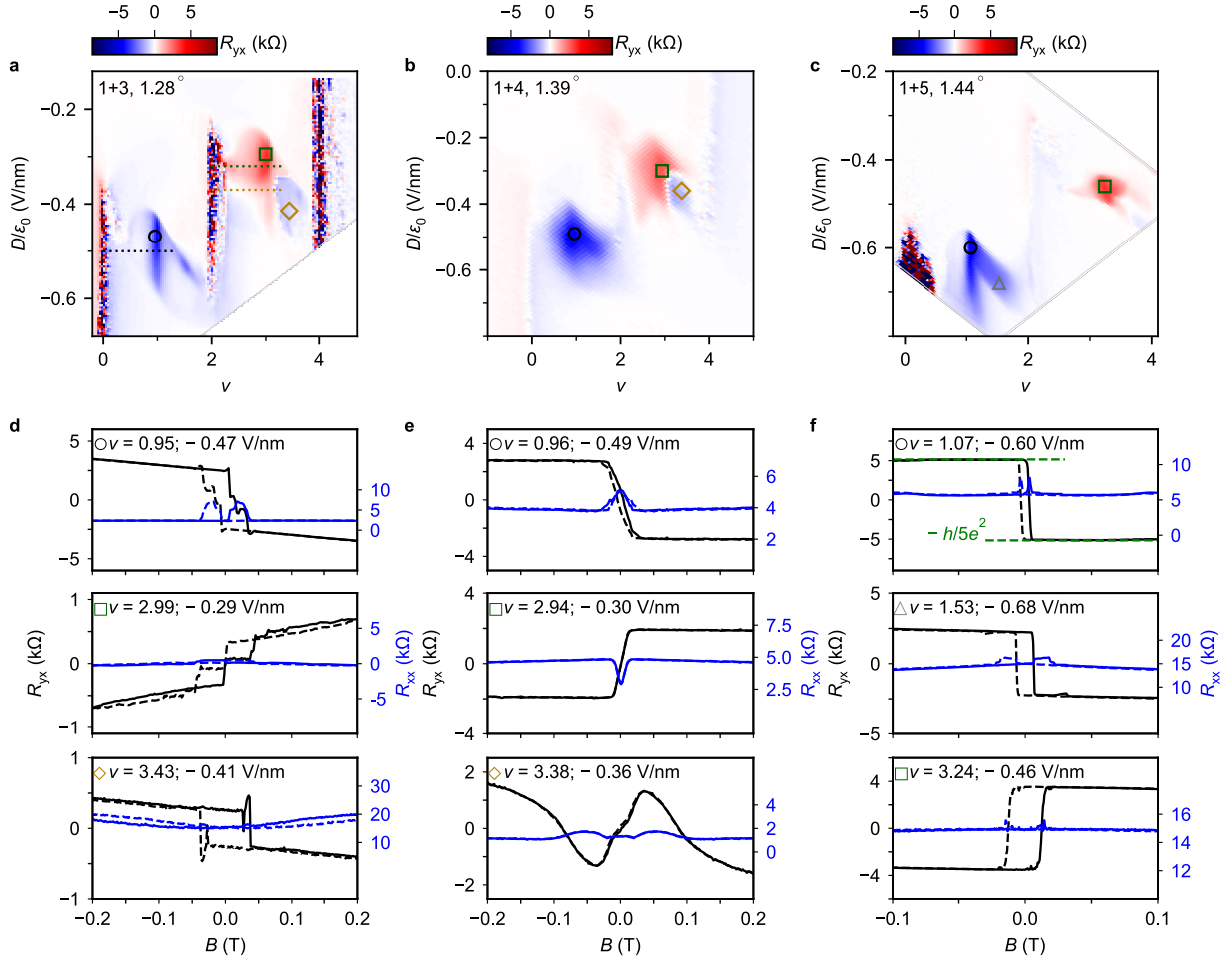


**Figure 3. Anomalous Hall and high-Chern-number quantum anomalous Hall effects.**  
**a-c**, Zoomed-in dual-gate maps of  $R_{yx}$  as a function of  $\nu$  and  $D/\varepsilon_0$  for (1+3), (1+4), and (1+5) devices. **d-f**,  $R_{yx}$  (antisymmetrized, black) and  $R_{xx}$  (symmetrized, blue) measured as a function of  $B$  for selected values of  $\nu$  and  $D/\varepsilon_0$ , which are labeled with corresponding markers in **a-c**. Solid (dashed) lines denote forward (backward)  $B$  sweeps. The (1+5) device displays a quantized plateau at  $|R_{yx}| = h/5e^2$ . All data were taken at  $T = 0.3$  K.

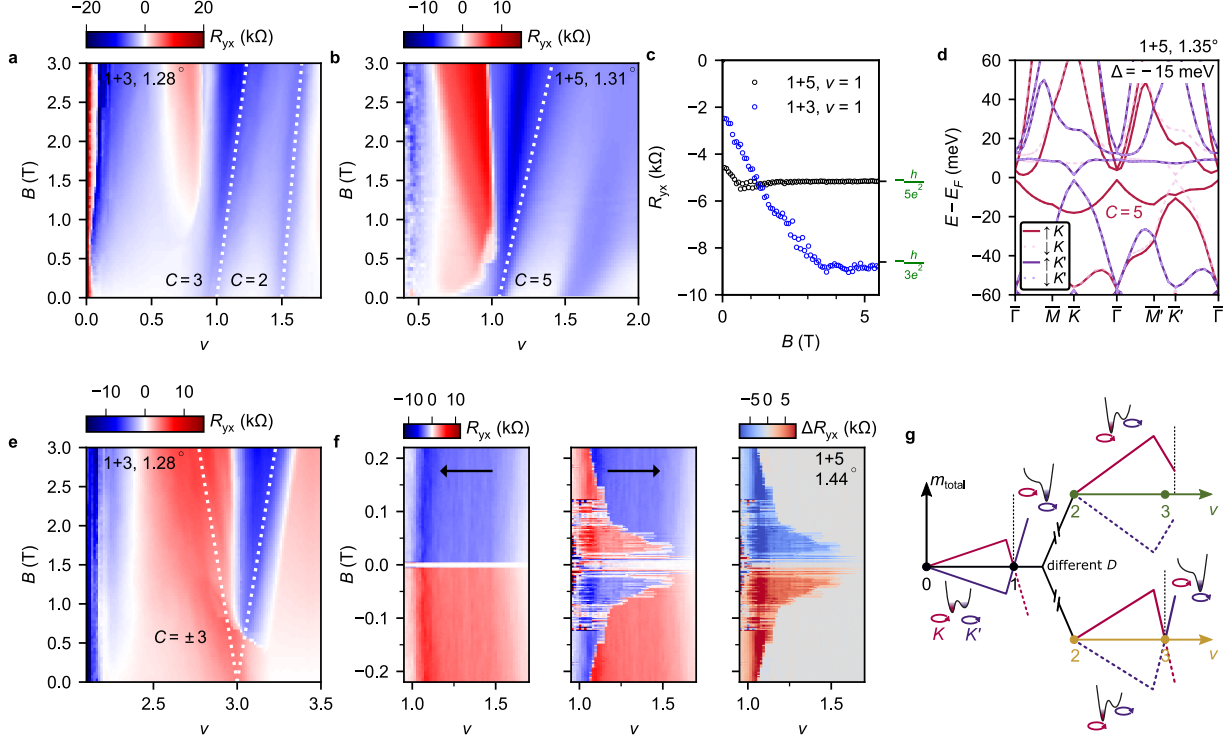


**Figure 4. Electrical and magnetic switching of high-Chern-number orbital magnets.** **a**,  $R_{yx}$  as a function of  $\nu$  and  $B$  for  $(1+3)$  device at  $D/\varepsilon_0 = -0.53$  V/nm. The dotted lines which correspond to the noted Chern numbers are drawn as a guide to the eye (same for **b** and **e**).  $T = 0.3$  K. **b**,  $R_{yx}$  as a function of  $\nu$  and  $B$  in a  $(1+5)$  device at  $D/\varepsilon_0 = -0.66$  V/nm.  $T = 0.3$  K. **c**, Linecuts in **a** and **b** along the dotted lines from  $\nu = 1$ . **d**, Hartree-Fock calculated band structure of  $1.35^\circ$ - $(1+5)$  graphene at  $\nu = 1$  and  $\Delta = -15$  meV, exhibiting spin-valley polarization at  $K\uparrow$  band with  $C = 5$ . **e**,  $R_{yx}$  as a function of  $\nu$  and  $B$  for  $(1+3)$  device at  $D/\varepsilon_0 = -0.29$  V/nm.  $T = 0.3$  K. **f**, Doping-induced magnetization switching in  $(1+5)$  device at  $D/\varepsilon_0 = -0.64$  V/nm.  $\nu$  scanned backward (left), forward (middle), and the difference between forward and backward scans (right).  $T = 0.05$  K. **g**, Schematic of doping-induced valley polarization switching. Red (purple) solid lines denote  $K$  ( $K'$ ) valley occupied, and dashed lines denote unoccupied valleys.  $x$ -axis:  $\nu$ .  $y$ -axis: total magnetization  $m_{\text{total}}$  of either valley. Within a partially filled band, only the bulk contribution evolves as a function of  $\nu$ , whereas when crossing a Chern gap, the edge current contribution appears while the bulk contribution remains constant. The three segments denote linecuts along  $\nu$  at different displacement fields (linecuts drawn in Fig. 3a with corresponding colors as an example).